Journal of the American Chemical Society is published by the American Chemical Society. 1155 Sixteenth Street N.W., Washington, DC 20036

J|A|C|S
ARTICLES

Chemical Control of Electronic Structure and Superconductivity in Layered Borides and Borocarbides: Understanding the Absence of Superconductivity in Li_xBC

Andrew M. Fogg, James Meldrum, George R. Darling, John B. Claridge, and
Matthew J. Rosseinsky*

Contribution from the Department of Chemistry, The University of Liverpool,
Liverpool, L69 7ZD United Kingdom

Received November 18, 2005; E-mail: m.j.rosseinsky@liv.ac.uk

Abstract: The synthetic search for materials related to the 39 K superconductor MgB_2 has been difficult. The most promising theoretical suggestion, hole doping of LiBC, does not lead to a new superconductor. We show here that a combination of density functional theory (DFT) calculations, materials synthesis, and structural characterization reveals the origin of the puzzling absence of superconductivity in $Li_{1/2}BC$ as a subtle change in the electronic structure driven by structural response to the introduction of holes. This indicates that the unique aspects of the electronic structure of MgB_2 will be demanding to replicate in other systems.

Introduction

MgB_2 has the highest superconducting transition temperature (39 K) for a noncuprate material.[1] The structure of MgB_2 consists of graphene-like B_2 sheets with Mg occupying the interlayer spaces. The remarkable T_c arises because the electronic structure of MgB_2 differs fundamentally from that of other isostructural metal diborides. In MgB_2, boron−boron bonding two-dimensional σ and three-dimensional π electronic states both occur at the Fermi level,[2,3] giving rise to a two-gap superconductor[4] in which both distinct types of carriers contribute to the high transition temperature. The material appears well-suited to subtle modification of this complex electronic structure by changing the carrier concentration via chemical substitution, but with the exception of Al,[5] Mn,[6] and C[7] doping, this has proved impossible due to the high thermodynamic stability of MgB_2.

The borocarbide LiBC[8] is isoelectronic with MgB_2 and adopts a similar hexagonal structure with alternating graphene BC and Li layers. The nodes of the graphene sheet are alternately occupied by B and C both between and within the BC sheets (Figure 1(i)). This decoration of the hexagonal layers opens a gap in the band structure and produces semiconducting rather than metallic behavior. Theoretical work[9] predicts that LiBC can be doped with holes (oxidized) by removal of Li to produce metallic behavior in the resulting Li_xBC ($x \leq 1$) systems. The calculations further show that the electronic structures of these doped systems display the same key feature of overlapping σ and π states at the Fermi energy that confers high T_c superconductivity on MgB_2. Quantitative analysis of the electron−phonon coupling leads to a predicted superconducting transition temperature in the range 65−105 K in $Li_{0.5}BC$.[9,10] As a result, the Li_xBC phase field has been the subject of detailed synthetic studies[11−15] which have not revealed superconductivity in any Li_xBC materials. In this paper, we use theory and experiment to identify the chemical and structural features limiting the extent to which Li can be removed from LiBC. From this analysis, a subtle interaction emerges between chemical, crystal, and electronic structure that drives the onset of energetically favorable exchange between B and C within the decorated BC graphene sheets in $Li_{0.5}BC$. This suppresses the similarity between the electronic structure of Li_xBC and MgB_2 and accounts for the absence of superconductivity in hole-doped Li_xBC.

Experimental Section

Synthesis. Table 1 summarizes the preparation conditions for the samples discussed in this paper. All of the reactions were performed in 6 cm long Ta tubes (Plansee Metals Ltd, 99.8%) coated with Mo

---

(1) Nagmatsu, J.; Nakagawa, N.; Muranaka, T.; Zenitani, Y.; Akimitsu, J. *Nature* **2001**, *21*, 410.

(2) An, J. M.; Pickett, W. E. *Phys. Rev. Lett* **2001**, *86*, 4366.

(3) Kortus, J.; Mazin, II.; Belashchenko, K. D.; Antropov, V. P.; Boyer, L. L. *Phys. Rev. Lett.* **2001**, *86* (20), 4656−4659.

(4) Choi, H. J.; Roundy, D.; Sun, H.; Cohen, M. L.; Louie, S. G. *Nature* **2002**, *418* (6899), 758−760.

(5) Slusky, J. S.; Rogado, N.; Regan, K. A.; Hayward, M. A.; Khalifah, P.; He, T.; Inumaru, K.; Loureiro, S. M.; Haas, M. K.; Zandbergen, H. W.; Cava, R. J. *Nature* **2001**, *410* (6826), 343−345.

(6) Cava, R. J.; Zandbergen, H. W.; Inumaru, K. *Physica* **2003**, (C 385), 8−15.

(7) Takenobu, T.; Ito, T.; Chi, D. H.; Prassides, K.; Iwasa, Y. *Phys. Rev. B* **2001**, *6413*, (13), art. no. 134513.

(8) Wörle, M.; Nesper, R.; Mair, G.; Schwarz, M.; Schnering, H. G. v. *Z. Anorg. Allg. Chem* **1995**, *621*, 1153.

(9) Rosner, H.; Kitaigorodsky, A.; Pickett, W. E. *Phys. Rev. Lett.* **2002**, *88*, article number 127001.

(10) Dewhurst, J. K.; Sharma, S.; Ambrosch-Draxl, C.; Johansson, B. *Phys. Rev. B* **2003**, *68* (2), art. no. 020504.

(11) Souptel, D.; Hossain, Z.; Behr, G.; Loser, W.; Geibel, C. *Solid State Commun.* **2003**, *125* (1), 17−21.

(12) Fogg, A. M.; Chalker, P. R.; Claridge, J. B.; Darling, G. R.; Rosseinsky, M. J. *Phys. Rev. B* **2003**, *67*, 245106.

(13) Fogg, A. M.; Claridge, J. B.; Darling, G. R.; Rosseinsky, M. J. *Chem. Commun.* **2003**, *12*, 1348−1349.

(14) Zhao, L.; Klavins, P.; Liu, K. *J. Appl. Phys.* **2003**, *93* (10), 8653−8655.

(15) Nakamori, Y.; Orimo, S. I. *J. Alloys Compd.* **2004**, *370*, (1−2), L7−L9.

10.1021/ja0578449 CCC: $33.50 © 2006 American Chemical Society

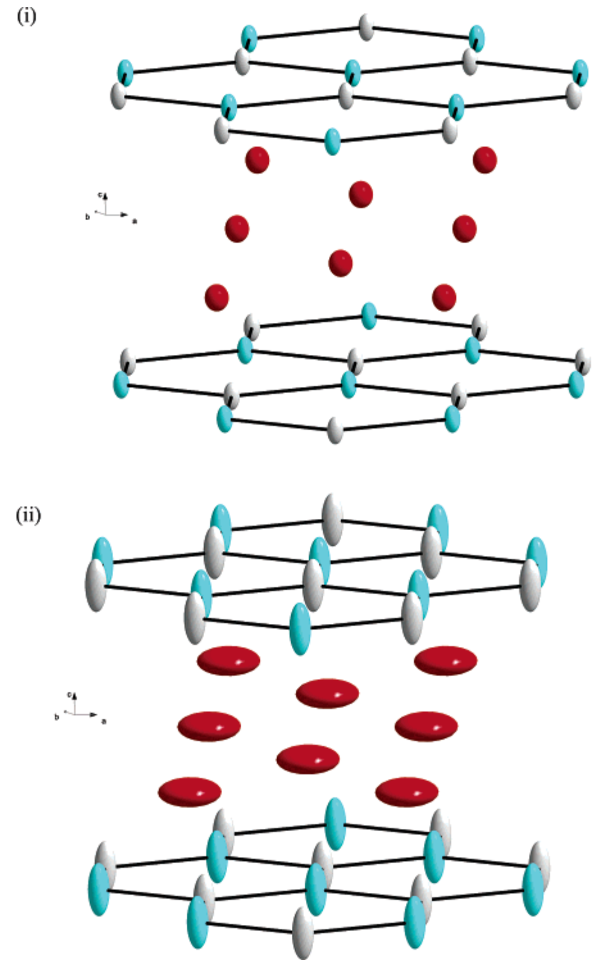

Figure 1. Refined average crystal structures of (i) LiBC and (ii) $Li_{0.56(2)}BC$ at 305 K. Li, red; B, gray; C blue. The atoms are represented by their anisotropic displacement parameter ellipsoids, with 70% probability ellipsoids shown in each case.

foil (Alfa Aesar, 99.95%) except where noted. Reagents used were Li (Alfa Aesar, 99.9%), amorphous B (Strem, 99+%, < 1 μm), C (Aldrich), and ^{11}B (Eagle-Picher, 99.52 at. %, < 22 μm). The Ta tubes are loaded in a helium-filled drybox and closed by argon arc welding. The ampules are heated in a tube furnace at 3 °C/min to 500 °C under a flow of argon. This temperature is maintained for the time specified in Table 1 before being raised at 3 °C/min to 1500 °C where the temperature is maintained for a further period as summarized in Table 1. The ampule is then cooled at a rate of 10 °C/min to room temperature. For the reactions where crystalline ^{11}B was used as a starting material instead of amorphous boron, the reactions were left at 500 °C for 2 h instead of 1 h due to the crystalline boron being less reactive due to its larger particle size. The starting composition corresponded to Li_3BC in all cases.

Powder Diffraction. Powder X-ray diffraction data for the initial characterization of all samples were collected on a Stoe Stadi-P instrument in Debye Scherrer geometry with Cu Kα_1 radiation and a linear position sensitive detector. Samples were sealed under helium in 0.5 or 0.3 mm capillaries and rotated about the capillary axis during data collection to minimize preferred orientation effects.

High-resolution powder X-ray diffraction data were collected on Station 9.1 of the U.K. Synchrotron Radiation Source at the Daresbury Laboratory on $Li_{0.16(1)}BC$ (X) (73% $Li_{0.21(1)}B_{0.73(1)}C_{1.27(1)}$ + 27% $B_{13}C_2$), on $Li_{0.67(4)}BC$ (V) (51% $Li_{0.38(5)}BC$ + 49% $Li_{0.97(3)}BC$), and on sample V annealed at 400 °C for 1 week in a silica tube under vacuum.

Variable temperature neutron powder diffraction data ($2 \leq T/K \leq 1100$) were collected on the GEM diffractometer[16] at the ISIS Spallation Source, Rutherford Appleton Laboratories, U.K. Data were collected for $Li_{0.36(2)}BC$ (VIII) (75% $Li_{0.50(2)}B_{0.70(1)}C_{1.30(1)}$ + 25% $B_{13}C_2$) for $5 \leq T/K \leq 305$ in 20 K intervals and $Li_{0.70(1)}BC$ (IV) (51% $Li_{0.41(2)}BC$ + 49% $Li_{1.000(5)}BC$) for $5 \leq T/K \leq 305$ in 50 K intervals. Data were collected for $Li_{0.79(2)}BC$ (III) (33% $Li_{0.56(2)}BC$ + 67% $Li_{0.904(8)}BC$) for $5 \leq T/K \leq 285$ in 10 K intervals. High-temperature data were collected for this sample and $Li_{0.67(1)}BC$ (VI) (51% $Li_{0.40(1)}BC$ + 49% $Li_{0.95(1)}BC$) at 298 K and $373 \leq T/K \leq 973$ at 100 K intervals. Data were also collected for $Li_{0.45(2)}BC$ (IX) (63% $Li_{0.38(1)}BC$ + 37% $B_{13}C_2$) at 2 K then from $10 \leq T/K \leq 290$ in 20 K intervals and from $373 \leq T/K \leq 973$ in 100 K intervals.

All of the powder diffraction data were analyzed using the GSAS suite of programs.[17] Quantitative analysis of the lab X-ray and synchrotron radiation data used neutral atom Li, B, and C form factors from the International Tables for Crystallography, Vol. IV. The displacement parameters for the B and C atoms were constrained to the same value after preliminary refinement had indicated their similarity. For the X-ray data, the atomic displacement parameters were refined isotropically in most cases as anisotropic refinements produced no improvement in the statistics. For sample XI (see below), however, there was a significant improvement in the fit parameters in the anisotropic refinement (anisotropic $\chi^2 = 3.762$, isotropic $\chi^2 = 3.823$). The neutron data were treated in a similar manner with additional consideration given to the displacement parameters and the absorption correction. For these data, anisotropic refinement of the B/C displacement parameters produced a significantly improved fit when compared to the isotropic refinements. For the Li site, refinements with anisotropic thermal parameters were less stable and did not yield significantly improved fit parameters when compared to the isotropic refinements. However, the anisotropic displacement parameters have been used for comparative purposes where stated. In these investigations, the absorption correction was refined within GSAS; comparison with refinement of analytically absorption-corrected data for the same sample demonstrated that the same results were obtained from the two different data analysis methods. Due to strong correlation between the absorption correction, lithium occupancy, and displacement parameters, they were initially refined alternately. After several cycles of refinement, stable refinements were possible with all of the parameters being refined simultaneously. The same results were obtained regardless of the order in which the parameters were refined.

Electron Diffraction. Samples for transmission electron microscopy (TEM) analysis were prepared by suspending a fine powder in acetonitrile. A drop of the suspension was then deposited onto a holey carbon grid, and the solvent was allowed to evaporate. Selected area electron diffraction (SAED) patterns were obtained by use of a double-tilting goniometer stage (±30 °) to tilt the specimen in a JEOL 2000 FX transmission electron microscope.

Additional samples were prepared for EELS by suspending a fine powder in dry hexane before depositing them on holey carbon grids analogously to above. EELS data were recorded on a Philips CM200ST microscope fitted with a Gatan Imaging filter at the University of Surrey.

Resistivity. Resistivity was measured using the DC transport option of a Quantum Design MPMS SQUID magnetometer. The current source was a Keithley 220 Programmable Current Source and the voltage source was a Keithley 2182 Nanovoltmeter. Standard four-point probe measurements were performed in the range $10 < T/K < 300$ for LiBC (I) and $5 < T/K < 300$ for $Li_{0.59(1)}BC$ (VII) (70% $Li_{0.43(1)}BC$ + 30% $Li_{0.96(3)}BC$). In both cases, X-ray powder data were recorded on the materials after the conductivity measurement, and they were unchanged. It was not possible to perform measurements on the highly Li deficient Li_xBC samples containing $B_{13}C_2$ due to their greater moisture sensitivity.

---

[16] Williams, W. G.; Ibberson, R. M.; Day, P.; Enderby, J. E. *Physica B* **1998**, *241−243*, 234−236.

[17] Larson, A. C.; Dreele, R. B. V. *GSAS: General Structural Analysis System*; Los Alamos National Laboratory: Los Alamos, NM, 1994.

Table 1. Summary of the Overall Sample (Li_mBC) and Constituent Phase (Li_xBC) Compositions of the Materials in this Study[a]

sample	overall Li_mBC sample composition	Li_xBC phase compositions and weight fractions within sample[b]	amounts of starting material used (g)			time at 500 °C (h)	time at 1500 °C (h)
			Li	B[c]	C		
I[d]	$Li_{1.00(1)}BC$	$Li_{1.00(1)}BC$	0.3225	0.18	0.185	2	1
II[d]	$Li_{0.90(2)}BC$	38% $Li_{0.83(2)}BC$ + 62% $Li_{0.95(2)}BC$	0.3225	0.18	0.185	2	6
III[d]	$Li_{0.79(1)}BC$	33% $Li_{0.56(2)}BC$ + 67% $Li_{0.904(8)}BC$	0.3225	0.18	0.185	2	24
IV	$Li_{0.70(1)}BC$	51% $Li_{0.41(2)}BC$ + 49% $Li_{1.000(5)}BC$	0.1075	0.06	0.0617	2	2
V	$Li_{0.67(4)}BC$	51% $Li_{0.38(5)}BC$ + 49% $Li_{0.97(3)}BC$	0.1075	0.06	0.0617	1	1
VI	$Li_{0.67(1)}BC$	51% $Li_{0.40(1)}BC$ + 49% $Li_{0.95(1)}BC$	0.1075	0.06	0.0617	2	6
VII	$Li_{0.59(2)}BC$	70% $Li_{0.43(1)}BC$ + 30% $Li_{0.96(3)}BC$	0.1075	0.06	0.0617	2	2
VIII	$Li_{0.36(2)}BC$	75% $Li_{0.50(2)}B_{0.70(1)}C_{1.30(1)}$ + 25% $B_{13}C_2$	0.1611	0.09	0.0925	2	12
IX	$Li_{0.27(2)}BC$	63% $Li_{0.45(2)}B_{0.49(1)}C_{1.51(1)}$ + 37% $B_{13}C_2$	0.0537	0.03	0.0308	2	6
X	$Li_{0.22(2)}BC$	86% $Li_{0.24(1)}B_{0.87(1)}C_{1.13(1)}$ + 14% $B_{13}C_2$	0.0537	0.03	0.0308	1	6
XI	$Li_{0.16(1)}BC$	73% $Li_{0.21(1)}B_{0.73(1)}C_{1.27(1)}$ + 27% $B_{13}C_2$	0.0537	0.03	0.0308	1	6

[a] The last four samples (below the separation) correspond to $m < 0.5$ and consist of $Li_xB_{1-y}C_{1+y}$ plus $B_{13}C_2$. The first seven samples (above the separation) have $m > 0.5$ and consist of coexisting Li_xBC phases. [b] The quoted Li compositions were obtained by refinement of the Li fractional occupancies with the data and methods described in the following section. [c] Samples II, VIII, IV, III, VI, and IX were synthesized from ^{11}B and refined from neutron powder diffraction data. [d] Prepared without Mo foil liners.

Samples were pressed into pellets and annealed at 800 °C for 20 h in silica tubes under vacuum. XRD post measurement showed that the samples were unchanged following the annealing procedure. The pellets were then cut into rectangular blocks and fixed onto the copper probe using varnish. Four needlelike copper electrodes were attached to the samples in a linear arrangement by application of a silver paste. Currents of 10 μA for LiBC (I) and 1 mA for $Li_{0.59(1)}BC$ (VII) (70% $Li_{0.43(1)}BC$ + 30% $Li_{0.96(3)}BC$) were used and measurements recorded every 1 K at a heating rate of 0.75 K/min.

Magnetization. Low-field measurements (40 G) were performed on all Li_xBC samples on a Quantum Design MPMS-XL SQUID magnetometer to search for evidence of superconductivity. There was no evidence of superconductivity in any of the samples above 2 K.

Elemental Analysis. Elemental analysis was used to confirm the Li contents of samples IV, VI, and IX For digestion, in each case, 10 mg of sample was added to a mixture of 2 mL of concentrated HNO_3, 1 mL of concentrated HF, and 1 mL of concentrated HCl and heated in a microwave at 10 °C/min to 210 °C at a pressure of 600 psi. This temperature and pressure were maintained for 10 min. Despite these extreme conditions, it was not possible to fully dissolve the samples. Analyses were carried out using ICP Optical Emission Spectroscopy on a SPECTRO CIROS CCD instrument. The elemental analysis data is summarized in Table S1 of the Supporting Information.

DFT Calculations. Density functional calculations have been performed with a plane-wave basis set, ultra-soft pseudopotentials, and the PBE version of GGA for exchange and correlation. Geometry optimizations were done using the CASTEP[18,19] package with an energy cutoff of 340 eV, whereas the density of states calculations were done with VASP4.6[20,21] with a cutoff of 286.7 eV. For the Li_xBC structures, the geometry, corresponding to a 3×3 supercell of the parent LiBC structure, was optimized in $P1$ symmetry using a Brillouin zone sampling of 14 special k points, with a final relaxation step using 32 k points. The unit cell does not distort significantly from hexagonal symmetry despite the absence of symmetry constraints. The density of states was calculated with 405 k points using the electron density obtained self-consistently with 32 k points.

Results

In the reported preparation of LiBC,[8] the Li is in a 3-fold excess and during the reaction serves as a flux, with excess lithium lost through the tube walls. By extending the time at which the samples are held at high temperature beyond the 1 h duration used in the original synthesis of LiBC and decreasing the ratio of sample to tube volume**,** samples of composition Li_mBC ($0.16 < m < 1$) can be prepared by high-temperature Li deintercalation from LiBC:[13] the latter modification of the reaction conditions to enhance deintercalation kinetics by varying the ratio of the reaction vessel volume to sample size gives access to lower overall Li contents than reported previously. As Li loss is controlled by the flux through the tube walls, the reduced sample volume in the same volume container is expected to lead to greater Li loss in a fixed reaction time as can be seen by, for example, comparing samples II and VI in Table 1 which have overall compositions of $Li_{0.90}BC$ and $Li_{0.67}BC$ respectively from the same reaction conditions. Using the Clausius−Clapeyron equation, the equilibrium vapor pressure of Li at 1500 °C was estimated to be 2.7 atm.

As these are dynamic, nonequilibrium reactions, it is very difficult to control the precise amount of Li present in the samples. It is, however, possible to identify trends within the syntheses. For example, a comparison of samples I−III reveals that for the same starting composition increasing the time at which the sample is held at 1500 °C leads to a decrease in the Li content of the sample. If a similar comparison is made between samples II and VI, it can be seen that as the initial amount of material in the Ta tube is reduced to one-third of its initial value then more Li deficient samples are formed in shorter times presumably as a result of a reduction in the pressure inside the tube. A further reduction in the amount of material to one-sixth of the initial amounts (sample IX) leads to even greater Li loss and the formation of the $B_{13}C_2$ byproduct under the same conditions. These trends are summarized in Tables S2 and S3 of the Supporting Information. It should also be noted that attempts to synthesize Li_xBC phases by stoichiometric combination of the elements were unsuccessful.

The lithium content in Table 1 is determined by Rietveld refinement of synchrotron X-ray and powder neutron diffraction data (Figure 2). The structures of all of the phases reported here were refined using the model reported previously for Li_xBC[22] which is based on that of LiBC with fractional occupation of the Li site. No evidence for the ordering of the Li atoms and vacancies is observed in any of the samples in either the powder

---

(18) Payne, M. C.; Teter, M. P.; Allan, D. C.; Arias, T. A.; Joannopoulos, J. D. *Rev. Mod. Phys.* **1992**, *64*, 1045.

(19) Milman, V.; Winkler, B.; White, J. A.; Pickard, C. J.; Payne, M. C.; Akhmatskaya, E. V.; Nobes, R. H. *Int. J. Quantum Chem.* **2000**, *77*, 895.

(20) Kresse, G.; Hafner, J. *Phys. Rev. B* **1993**, *47*, 558.

(21) Kresse, G.; Furthmuller, J. *Phys. Rev. B* **1996**, *54*, 11169.

(22) Fogg, A. M.; Claridge, J. B.; Darling, G. R.; Rosseinsky, M. J. *Chem. Commun.* **2003**, *12*, 1348−1349.

Table 2. Crystallographic Data from Refinement of the Room Temperature Neutron Diffraction Data Collected on GEM for the Li_xBC Samples[a]

phase			$Li_{0.40}BC$	$Li_{0.41}BC$	$Li_{0.56}BC$	$Li_{0.83}BC$	$Li_{0.90}BC$	$Li_{0.95}BC$	$Li_{0.95}BC$	LiBC	LiBC	$Li_{0.45(2)}B_{0.49}C_{1.51}$	$Li_{0.50(2)}B_{0.70}C_{1.30}$
sample			VI	IV	III	II	III	VI	II	IV	I	IX	VIII
temp (K)			290	305	285	285	285	290	285	305	285	290	305
unit cell dimensions	a/ Å		2.5922(1)	2.5793(3)	2.6267(12)	2.74496(9)	2.72687(5)	2.72854(9)	2.73665(7)	2.75237(7)	2.74798(1)	2.5325(2)	2.56580(8)
	c/Å		7.5604(6)	7.6123(14)	7.4427(7)	7.0533(2)	7.1099(3)	7.0881(3)	7.0771(2)	7.0618(3)	7.04798(5)	7.5715(7)	7.6281(4)
	V/ Å^3		43.998(5)	43.858(9)	44.741(4)	46.025(1)	45.785(2)	45.701(4)	45.901(1)	46.330(2)	46.092(1)	42.056(6)	43.490(3)
displacement parameters	B/C[b]	$U_{11,22}$/ Å^2	0.0071(6)	0.0033(8)	0.0046(4)	0.00225(6)	0.0044(2)	0.0032(3)	0.00386(6)	0.0024(5)	0.00305(3)	0.0018(3)	0.0042(5)
		U_{33}/ Å^2	0.0131(8)	0.0072(13)	0.029(1)	0.00605(9)	0.0066(3)	0.0080(5)	0.00679(9)	0.0082(7)	0.00602(6)	0.0177(7)	0.0125(6)
		U_{12}/ Å^2	0.0035(2)	0.0016(4)	0.0023(2)	0.00112(3)	0.0022(1)	0.0016(2)	0.00193(3)	0.0014(2)	0.00152(2)	0.0009(1)	0.0021(2)
	Li	U_{iso}/ Å^2	0.014(3)	0.005(4)	0.031(4)	0.0102(7)	0.0105(8)	0.0075(9)	0.0116(8)	0.006(1)	0.00956(3)	0.030(5)	0.039(5)
fractional occupancies	f_{Li}		0.40(1)	0.41(2)	0.56(2)	0.83(2)	0.90(1)	0.95(1)	0.95(1)	1.05(2)	1.00(1)	0.45(2)	0.50(2)
	χ^2		2.943	1.020	1.266	8.055	1.266	2.943	8.055	1.020	4.974	3.461	2.011
	R_f2	bank 4	0.0760	0.0735	0.0691	0.0570	0.0691	0.0760	0.0570	0.0735	0.0918	0.0415	0.0651
		bank 5	0.0788	0.0807	0.1662	0.0759	0.1662	0.0788	0.0759	0.0807	0.1241	0.0469	0.0966
		bank 6	0.1361	0.2208	0.1308	0.1236	0.1308	0.1361	0.1236	0.2208	0.1386	0.0588	0.1355
	R_{wp}	bank 4	0.0698	0.0492	0.0432	0.0614	0.0432	0.0698	0.0614	0.0492	0.0497	0.0560	0.0630
		bank 5	0.0732	0.0451	0.0429	0.0491	0.0429	0.0732	0.0491	0.0451	0.0397	0.0645	0.0635
		bank 6	0.0717	0.0333	0.0344	0.0521	0.0344	0.0717	0.0521	0.0333	0.0541	0.0412	0.0389

[a] All refinements were carried out in space group $P6_3/mmc$ with Li (2*a*) at (0,0,0), B (2*c*) at (1/3,2/3,3/4), and C (2*d*) at (1/3,2/3,1/4). Refinement figures are shown in the Supporting Information. [b] The displacement parameters for B and C were constrained to be the same.

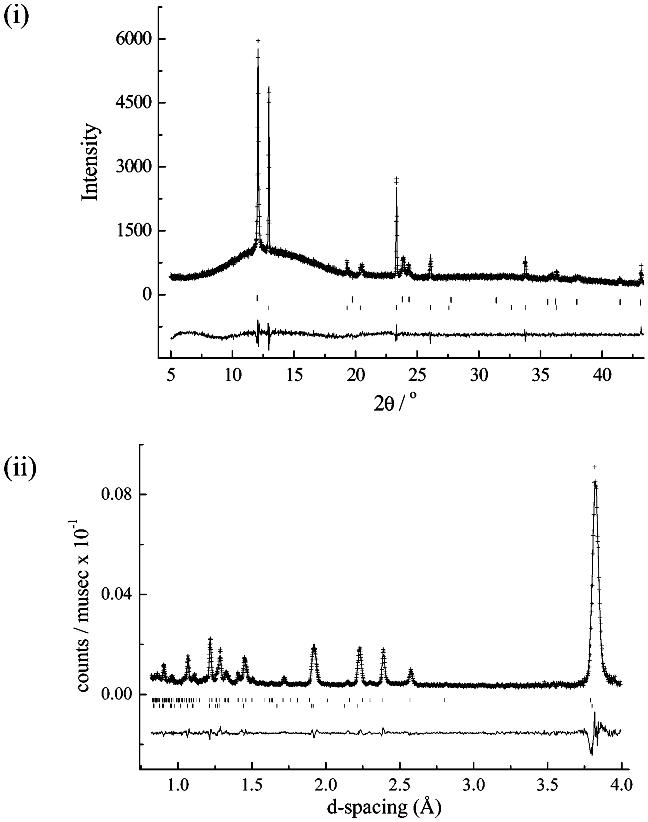

Figure 2. (i) Observed, calculated, and difference patterns from the Rietveld refinement of sample V (overall composition $Li_{0.67(4)}BC$: 51% $Li_{0.38(5)}BC$ (upper tick marks) + 49% $Li_{0.97(3)}BC$) annealed at 400 °C. The data were collected on Station 9.1 of the U.K. SRS, Daresbury Laboratory at a wavelength of 0.7972 Å. Refined parameters are given in Table 3. (ii) The observed, calculated, and difference patterns from the Rietveld refinement of neutron diffraction data for sample VIII of overall composition $Li_{0.16(1)}BC$ (75 wt % $Li_{0.50(2)}B_{0.70(1)}C_{1.30(1)}$ (lower tick marks) + 25 wt % $B_{13}C_2$). The data shown are from bank 4 ($2\theta = 63.62°$) of GEM. Refined parameters are given in Table 2.

diffraction data or from electron diffraction. Annealing of the samples, at temperatures up to 600 °C, makes no discernible difference to the diffraction patterns. The materials divide into two families differing in their compositional and structural response to Li loss and are usefully classified by the overall Li_mBC sample composition resulting from the Li_xBC phases and other phases present. Phase (Li_xBC) and overall sample (Li_mBC) compositions resulting from the starting compositions in each case are given in Table 1.

The refined structures of both families of phases are usefully discussed with reference to the structure of LiBC, refined here from powder neutron data using the same strategy as applied to the new Li_xBC phases. The 300 K refined displacement parameters for all atoms in the present powder neutron study compare well with the original single-crystal X-ray refinements for LiBC, demonstrating that the treatment of absorption here is satisfactory and that reliable displacement parameters can be extracted from two-phase powder samples due to the considerable separation in cell parameters; this is significant as the displacement parameters are later used to draw conclusions concerning static atomic displacements which are then compared with DFT calculations. The 5 K refinement affords almost isotropic displacement parameters for the B/C sheet in LiBC. The Li displacement ellipsoid is also best described isotropically.

Table 3. Crystallographic Data from Refinement of the Room Temperature Laboratory and Synchrotron X-ray Radiation Data for Li_xBC[a]

phase			$Li_{0.38}BC$	$Li_{0.43}BC$	$Li_{0.97}BC$	$Li_{0.96}BC$	$Li_{0.24(1)}B_{0.87}C_{1.13}$	$Li_{0.213(9)}B_{0.73}C_{1.27}$
sample			V	VII	V	VII	X	XI
instrument			9.1, SRS	Stoe	9.1, SRS	Stoe	Stoe	9.1, SRS
unit cell dimensions	a/ Å		2.5845(2)	2.5935(4)	2.7433(1)	2.7349(3)	2.5620(2)	2.5378(2)
	c/Å		7.5667(7)	7.565(2)	7.0645(5)	7.097(2)	7.6135(2)	7.5857(2)
	V/ Å^3		43.771(9)	44.07(2)	46.044(6)	45.97(2)	43.278(5)	42.309(5)
displacement parameters	B/C	U_{iso}/ Å^2	0.006(3)	0.008(2)	0.006(1)	−0.004(3)	0.0035(8)	-
	B/C[b]	$U_{11,22}$/ Å^2						0.0144(9)
		U_{33}/ Å^2						0.079(6)
		U_{12}/ Å^2						0.0072(5)
	Li	U_{iso}/Å^2	0.04(2)	0.03(1)	0.001(4)	0.005 (fixed)[c]	0.03 (fixed)[c]	0.03(fixed)[c]
fractional occupancies	f_{Li}		0.38(5)	0.43(1)	0.97(2)	0.96(3)	0.24(1)	0.213(9)
	χ^2		2.687	1.042	2.687	1.042	2.364	3.773
	R_{f^2}		0.1825	0.4995	0.1825	0.4995	0.1514	0.119
	R_{wp}		0.1006	0.1750	0.1006	0.1750	0.0883	0.0665

[a] All refinements were carried out in space group $P6_3/mmc$ with Li (2*a*) at (0,0,0), B (2*c*) at (1/3,2/3,3/4), and C (2*d*) at (1/3,2/3,1/4). Refinement figures are shown in the Supporting Information. [b] The displacement parameters for B and C were constrained to be the same. [c] For samples X and XI and one component of sample VII, it was necessary to fix the Li displacement parameter in order to obtain a stable and physically reasonable refinement. This was done at values consistent with those obtained from comparable compositions in the neutron refinements above.

The refined crystallographic parameters for all the phases are summarized in Tables 2 and 3. The variations of the lattice parameters, *a* and *c*, and the unit cell volume with refined Li content for the Li_xBC phases at room temperature are shown in Figure 3. From the data, it can be seen that both the unit cell volume and *a* decrease steadily with decreasing Li content while *c* increases, indicating that the loss of Li is weakening the interlayer interactions. If the plots are redrawn using diffraction data collected at 5 and 973 K (see Figures S1 and S2 in the Supporting Information) the variation of *a*, *c*, and *V* with Li follows similar trends. Elemental analysis was used to confirm the refined Li contents of the samples. It was found that those with a lower refined Li content did contain less Li although all of the experimental values were consistently lower than those calculated from the refined compositions as a result of the poor solubility of the materials.

The samples with the lowest overall Li contents ($m < 0.5$) consist of a hexagonal phase with the layered LiBC-type structure in the presence of significant quantities of expelled boron in the form of $B_{13}C_2$. The presence of the two phases is confirmed by the selected area electron diffraction patterns (Figure 4) which clearly show both the hexagonal LiBC-like and the tetragonal $B_{13}C_2$ phase. Particles of the hexagonal phase, which have an irregular platelike habit, show diffuse patterns for the [0001] projection. However, when tilted, no appreciable change is observed, indicating rodlike diffraction features in reciprocal space and significant layer stacking disorder within the crystals along *c*. No amorphous material is observed in these samples in the TEM, and the compositions of the resulting layered phases are thus carbon-rich, e.g., $Li_{0.45(2)}B_{0.49(1)}C_{1.51(1)}$ for sample IX as determined from the initial composition and the refined quantity of $B_{13}C_2$ in the product. Close inspection of the X-ray diffraction data for samples VIII−XI which feature boron expulsion reveals that the (101) reflection of the Li_xBC-like phase is absent even in a long data collection on the Stoe Stadi-P instrument over the 2θ region where it is expected. This refinement is shown in Figure S3. In LiBC the (101) reflection, and odd *l* reflections in general, results from the strict alternation of B and C along the *c* axis, and its absence in these materials could result from either an *AAA* stacking sequence or from a disordered model in which the additional C atoms occupy the B site. In both cases, the symmetry would be increased to $P6/mmm$ from $P6_3/mmc$ with the *c* axis halved. Refinements were performed in both space groups, and the parameters for sample XI are compared in Table S4. The refinement statistics indicate that the original $P6_3/mmc$ model is a better fit to the data. The absence of the (101) reflection may therefore result from a combination of the poor crystallinity of the sample and the reduction in the already weak contrast between the B and C atoms in data brought about by the presence of some C on the B site. It is therefore concluded that layer alternation is retained in the highly Li-deficient phases, which may be C rich.

It should be noted that both X-ray and neutron scattering lengths of ^{11}B and C are sufficiently similar to prevent their distinction by these techniques on grounds other than chemical environment. The displacement parameters for Li are an order of magnitude larger (Table 4) for these B-deficient/C excess phases than for LiBC itself, whereas the B/C atoms display consistently enhanced out-of-plane anisotropy compared with the parent phase. It is found from polynomial analysis of the temperature dependence that the displacement parameters have a large temperature independent component, and this will be discussed below.

Confirmation that samples VIII−XI are indeed boron deficient and of the general formula $Li_xB_{1-y}C_{1+y}$ was obtained by EELS measurements on sample X and one comparable to sample III. These investigations revealed that a graphite-like environment is maintained in both samples, as indicated by the shape of the EELS spectra, and that the B:C ratio was 0.34:1 in sample X and 1:1 within error in the other sample. Although the variation in the B:C ratio found by EELS for sample X is greater than that predicted by the diffraction studies, it is a clear demonstration that lower levels of Li in the materials are compensated for by an increase in the carbon content of the layers. The EELS spectra and deconvoluted data are shown in Figure S4.

The samples with higher overall Li contents ($m > 0.5$) consist of two coexisting Li_xBC phases with different *x* values but with no $B_{13}C_2$ or other B-containing second phase. It is notable from Figure 3 that the compositions of the component phases of these biphasic samples cluster into Li-rich ($x \approx 0.9$) and Li-poor ($x \approx 0.5$) compositions, with no intermediate unit cell volumes and accompanying refined Li contents observed. In this family, tilting of the particles in electron diffraction away from the [0001] zone axis yielded other projections, indicating retention of the coherent BC layer stacking found for LiBC itself, in contrast to the B-deficient materials found at lower overall Li

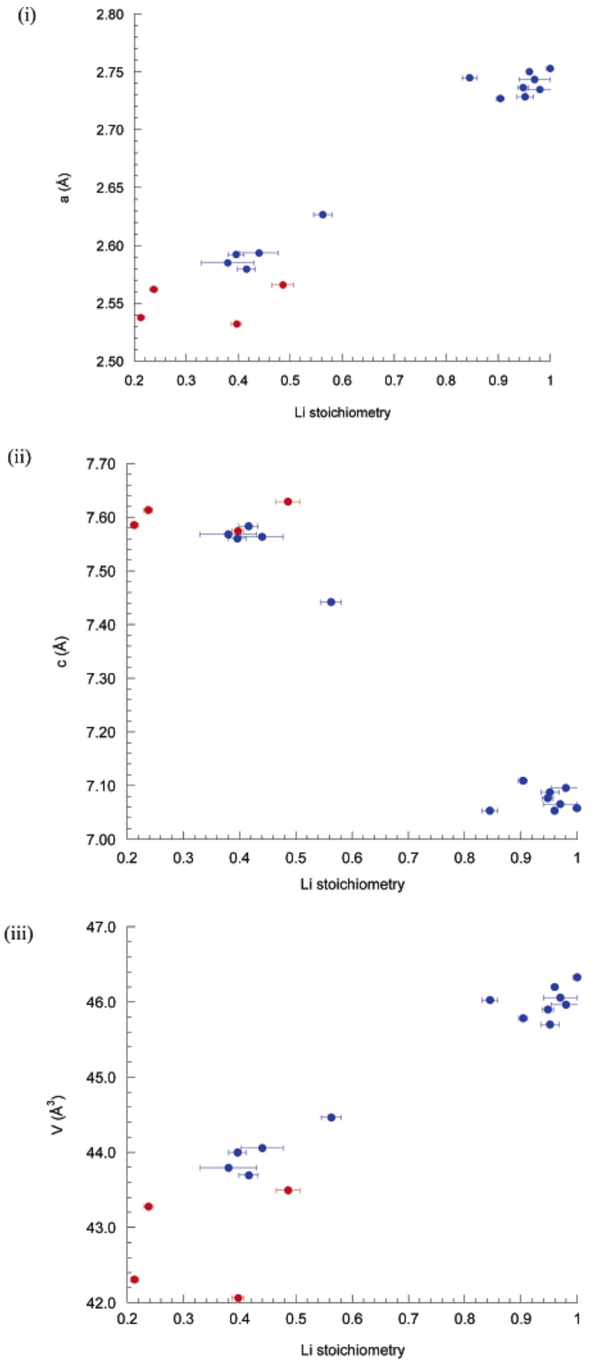

Figure 3. Variation of (i) a, (ii) c, and (iii) unit cell volume V with refined Li content x in Li_xBC (blue, samples I−VII) and $Li_xB_{1-y}C_{1+y}$ (red; $0.26 < y < 0.51$, samples VIII−XI) at room temperature. Note that with the exception of $Li_{1.00(1)}BC$ (sample I) the phases occur in samples that are biphasic mixtures: the blue points correspond to samples consisting of two Li_xBC phases with different x values, whereas the red points correspond to samples consisting of $B_{13}C_2$ plus a single B-deficient hexagonal $Li_xB_{1-y}C_{1+y}$ phase.

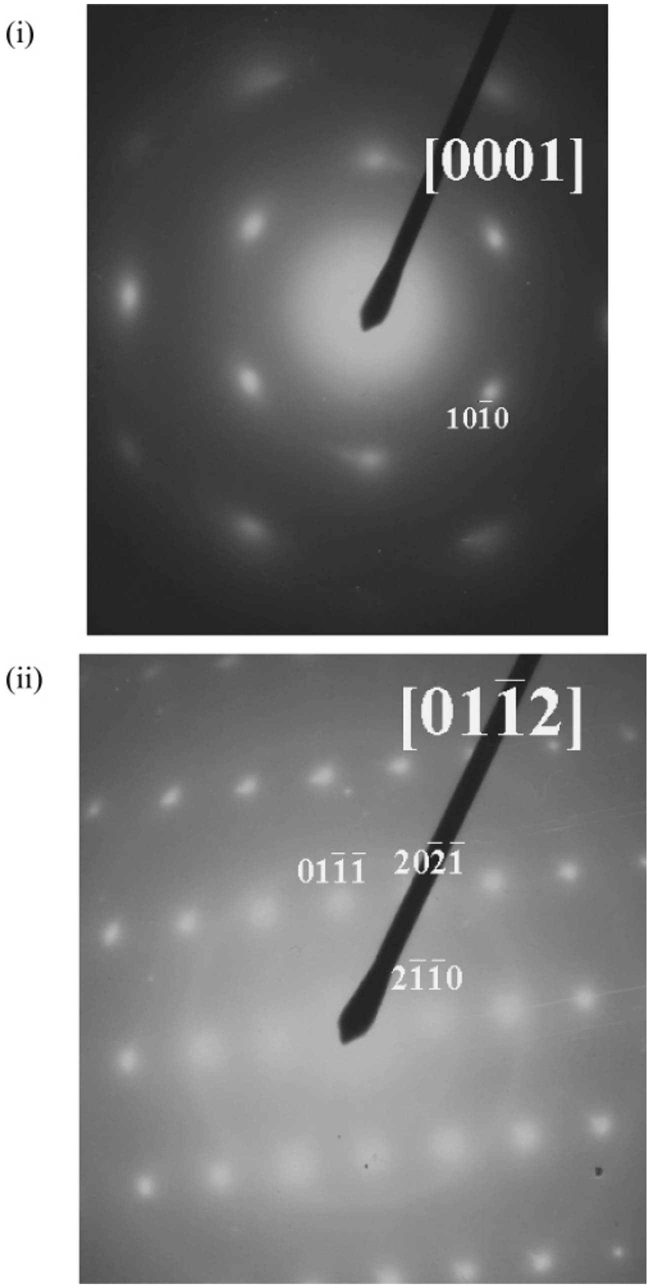

Figure 4. Selected area electron diffraction patterns for the two phases present in sample VIII (i) $Li_{0.50(2)}B_{0.70(1)}C_{1.30(1)}$ and (ii) $B_{13}C_2$.

Table 4. Refined Displacement Parameters from Powder Neutron Diffraction Data at 5 K for Samples VIII, IV, and III and 2 K for Sample IX[a]

phase	Li U_{iso} (Å^2)	B/C $U_{11,22}$(Å^2)	B/C U_{33} (Å^2)	B/C U_{33}/U_{11}
LiBC (IV)	0.0020(9)	0.0043(4)	0.0047(5)	1.09
$Li_{0.90}BC$ (III)	0.0059(7)	0.0046(2)	0.0043(2)	0.93
$Li_{0.56}BC$ (III)	0.024(3)	0.0042(3)	0.023(1)	5.48
$Li_{0.41}BC$ (IV)	0.012(4)	0.0031(6)	0.0058(4)	1.87
$Li_{0.45}B_{0.49}C_{1.51}$ (IX)	*0.028(3)*	*0.0017(2)*	*0.0129(6)*	*7.59*
$Li_{0.50}B_{0.70}C_{1.30}$ (VIII)	*0.029(2)*	*0.0035(2)*	*0.0082(4)*	*2.34*

[a] The C-rich samples in the materials with $B_{13}C_2$ second phase are italicized.

contents. It is important to note that the atmospheric stability of the two families of materials is distinct: X-ray diffraction following exposure to laboratory air reveals that the highly Li-deficient materials with coexisting Li_xBC and $B_{13}C_2$ decompose rapidly into amorphous products when exposed to air, whereas the materials consisting of two coexisting Li_xBC phases can survive at least 30 min exposure without decomposition.

There is no evidence in the low temperature neutron diffraction data for any ordering of the vacancies and Li atoms between the layers or for long-range ordered deformation of the layers. In all of the refinements of the neutron diffraction data, the Li displacement parameters were refined isotropically, whereas

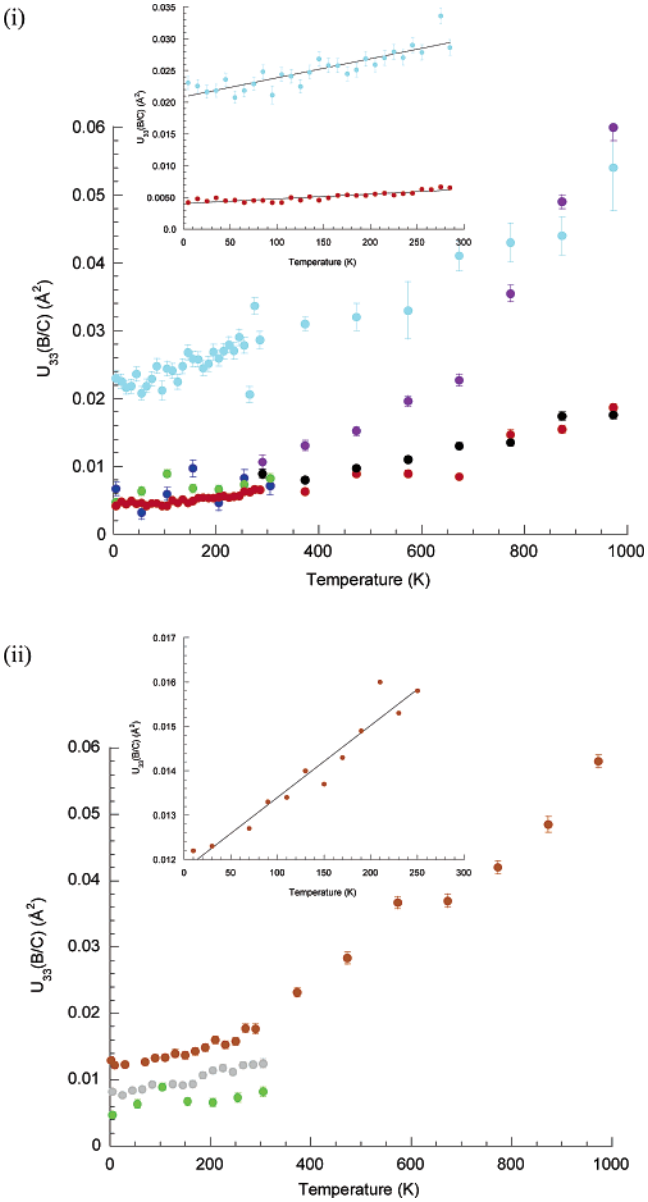

Figure 5. (i) Temperature dependence of U_{33}(B/C) for the Li$_x$BC phases (Li$_{0.40}$BC (VI, purple dots), Li$_{0.41}$BC (IV, dark blue dots), Li$_{0.56}$BC (III, light blue dots), Li$_{0.90}$BC (III, red dots), Li$_{0.95}$BC (VI, black dots), LiBC (IV, green dots)) The inset shows a first-order polynomial fit to the low-temperature data for Li$_{0.56}$BC and Li$_{0.90}$BC. (ii) Temperature dependence of U_{33}(B/C) for the Li$_x$B$_{1-y}$C$_{1+y}$ phases (LiBC (IV, green dots), Li$_{0.50}$B$_{0.70}$C$_{1.30}$ (VIII, gray dots), and Li$_{0.45}$B$_{0.49}$C$_{1.51}$ (IX, red dots). The inset shows a first-order polynomial fit to the low-temperature data for Li$_{0.45}$B$_{0.49}$C$_{1.51}$.

those for the B and C atoms in the layers were constrained to be the same and refined anisotropically. The temperature dependence of the U$_{33}$ components of the anisotropic displacement parameters for the B/C sheets for Li$_x$BC phases in samples III, IV, and VI are shown in Figure 5(i) and those for Li$_x$B$_{1-y}$C$_{1+y}$ phases in samples VIII and IX in Figure 5(ii). Data for U$_{11}$(B/C) and U$_{iso}$(Li) are available in the Supporting Information (Figures S5 and 6). Table 4 summarizes the data at the lowest temperature recorded for each phase.

The more Li deficient samples have higher values of the Li displacement parameter, with a maximum seen for compositions close to Li$_{0.5}$BC. This suggests increased static disorder in these materials as the number of lithium vacancies increases. If the Li displacement parameters are refined anisotropically, then it is found that at compositions close to $x = 1.0$ the in-plane and out-of-plane vibrational amplitudes remain similar to each other ($U_{11} = 0.0058(18)$ Å^2 and $U_{33} = 0.0074(33)$ Å^2 for Li in LiBC (IV)). In the more Li deficient phases, the values for U_{11} are larger than those for U_{33} indicating that the displacement amplitudes for Li are greater parallel to the layers. In Li$_{0.56}$BC (III), for example, values of $U_{11} = 0.041(7)$ Å^2 and $U_{33} = 0.008(13)$ Å^2 are calculated, and the refinement statistics are similar to those in the isotropic treatment which are reported in Table 3. Figure 1 shows the refined structure and anisotropic displacement parameters for LiBC and Li$_{0.56}$BC.

The contribution of the static disorder to the displacement parameters can be evaluated by extrapolation of a first-order polynomial fit to their temperature dependence to 0 K. This extrapolation of the isotropic displacement parameters for Li to 0 K shows that the static component is significantly greater for the phases which have a composition close to $x = 0.5$ rather than those closer to $x = 1$ (LiBC (IV) 0.0025(9) Å^2, Li$_{0.9}$BC (III) 0.0060(3) Å^2, Li$_{0.56}$BC (III) 0.029(2) Å^2, Li$_{0.41}$BC (IV) 0.011(4)) Å^2. In each case for the more Li deficient phases, $x = 0.41$ and 0.56, the temperature dependence is zero within error, whereas it is small for the other phases (LiBC (IV): $\partial U/\partial T = 1.4(6) \times 10^{-5}$ Å^2 K^{-1}; Li$_{0.9}$BC (III): $\partial U/\partial T = 1.2(2) \times 10^{-5}$ Å^2 K^{-1}).

The anisotropic displacement parameters for the B/C sheets show the expected increases with temperature although the temperature dependence is much more pronounced out of the plane of the sheets. The B/C displacement parameters for samples with Li compositions of around $x = 0.5$ are generally larger than those where composition is closer to $x = 1.0$. The anisotropy of the displacement ellipsoids increases significantly once the Li stoichiometry drops below 0.9 when the out-of-plane displacements become dominant as can be seen from the U_{33}/U_{11} ratios reported in Table 4 and the ORTEP diagrams in Figure 1. This is in contrast to the observations for the Li sites. Similar trends are observed if the ratios are calculated at 100, 290, and 973 K.

To minimize the effect of absorption on comparison of the displacement parameters for differing x values, the parameters for the Li$_{0.56}$BC and Li$_{0.90}$BC components of sample III can be considered; as both phases form part of the same sample, the same absorption correction is applied in both cases. The contribution of the static disorder to the displacement parameters can be evaluated by the first-order polynomial extrapolation of their temperature dependence to 0 K as was done for the Li displacements. The static components of the U$_{33}$ thermal displacements can thus be estimated as 0.0217(6) Å^2 and 0.0041(1) Å^2 for the Li$_{0.56}$BC and Li$_{0.90}$BC phases of sample III, respectively (see the inset of Figure 5). Treating the data for U_{11} in a similar way yields values of 0.0046(2) Å^2 and 0.0042(1) Å^2, respectively, and gives U_{33}/U_{11} ratios of 4.72 and 0.98 for Li$_{0.56}$BC and Li$_{0.90}$BC, respectively. These numbers confirm the increased displacement anisotropy of the more Li deficient phases and indicate that it is due to an increasing static component to the displacements. This provides an indication of localized static deformations around the vacancies in the structure. The thermal evolution of the displacement parameters is the same within error for U_{11} ($\partial U_{11}/\partial T = 2.1 \times 10^{-6}$ Å^2 K^{-1}), but the thermal variation of U_{33} is greater for Li$_{0.56}$BC

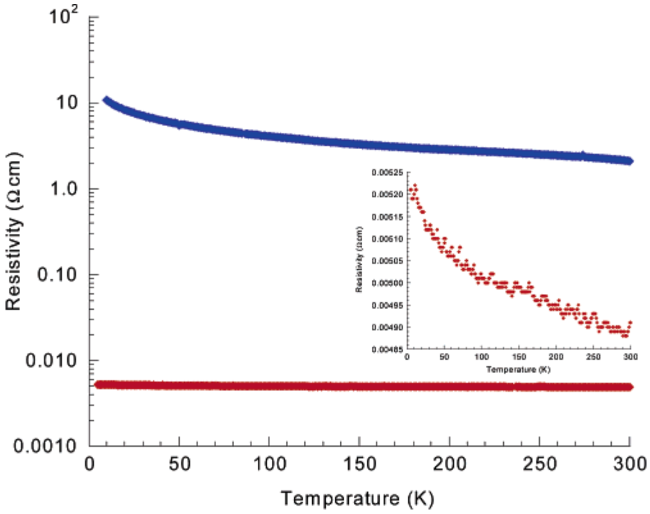

Figure 6. Temperature dependence of the resistivity of biphasic $Li_{0.59(2)}BC$ (70% $Li_{0.43(1)}BC$ + 30% $Li_{0.96(3)}BC$; sample VII, red) and LiBC (blue) represented on the same logarithmic scale. The inset shows that the resistivity of sample VII increases by 6% between 300 and 5 K.

($\partial U_{33}/\partial T = 2.0(5) \times 10^{-5}$ Å^2 K^{-1}) than $Li_{0.90}BC$ ($\partial U_{33}/\partial T = 6.5(8) \times 10^{-6}$ Å^2 K^{-1}).

The same analysis for the B-deficient phase $Li_{0.45(2)}B_{0.49(1)}C_{1.51(1)}$ from sample IX reveals similar trends. The static component of the U_{33} thermal displacement parameter is 0.0120(3) Å^2, whereas that for U_{11} is 0.0015(1) Å^2, and the ratio of $U_{33}/U_{11} = 8.0$. These numbers indicate that although the static components are smaller for the B deficient materials there is a greater displacement anisotropy than for those with a 1:1 ratio of B:C. From the gradients of the plots, it is evident that U_{11} is temperature independent within error and that U_{33} has $\partial U_{33}/\partial T = 1.6(2) \times 10^{-5}$ Å^2 K^{-1} which is comparable to thermal evolution of the parameter for the Li_xBC phases of a similar composition. Analogous treatment of the data for U_{iso}(Li) reveals a static component of 0.027(1) Å^2 and a gradient of $\partial U/\partial T = 1.5(7) \times 10^{-6}$ Å^2 K^{-1} which are in broad agreement with those obtained for the Li_xBC phases with similar Li compositions. The extent of doping-induced static distortion of the B-deficient phases is demonstrated by the observation that anisotropic displacement parameters are required for the satisfactory refinement of X-ray data from the $Li_{0.213(9)}B_{0.73}C_{1.27}$ component of sample X, in contrast with the X-ray data for all other samples studied.

Magnetization measurements reveal that none of the samples are superconducting above 2 K. The temperature dependence of the resistivity of LiBC (sample I) exhibits semiconducting characteristics and is shown in Figure 6.

The data show a 5-fold increase in resistivity over the measured temperature range with a room-temperature value of 2.1 Ω cm. This can be compared to values of 2.5 and 0.1 Ω cm reported in previous studies.[23] The latter was recorded on a quasi-single-crystal, and therefore, the smaller value is probably due to a reduction in the number of grain boundaries in comparison to our sample. The data cannot be fitted to either thermally activated behavior ($\rho \propto \exp(E/T)$) or a variable range hopping model ($\rho \propto \exp(B/T^{1/4})$) which is in agreement with the previous quasi-single-crystal measurements. The data are best fitted by a power law, $\rho \propto T^{-n}$, which gives a value of $n = 0.487(2)$ which is double the value of $n \approx 0.23$ that has been determined previously for LiBC.

The resistivity of sample VII of $Li_{0.59(2)}BC$ (70% $Li_{0.43(1)}BC$ + 30% $Li_{0.96(3)}BC$ (Figure 6) is 3 orders of magnitude smaller than LiBC (in either the previous quasi-single-crystal or present pellet measurements) and shows very little temperature dependence (Figure 6 inset). These data were confirmed by a second measurement on a sample of similar composition. This increase in conductivity indicates that the Li deficient phases are highly conducting, consistent with the original DFT predictions[2] of significant density of states at the Fermi level.

The present DFT calculations qualitatively reproduce the contraction of the in-plane lattice parameter *a* and the increase in out-of-plane lattice parameter *c*. DFT relaxation of vacancy-containing supercells with different Li distributions for the $Li_{0.5}BC$ composition consistently reveals significant layer puckering with a period sufficiently long for local planarity at the B and C atoms to be conserved. (Figure 7).

The calculations do not reveal significant energy gains for Li ordering. The B−C bond length decreases slightly from 1.565 Å for LiBC to 1.54 ± 0.02 Å, consistent with the decrease in *a*, whereas the rms deviations from planarity range from 0.067 to 0.082 Å depending on the details of the Li distribution. In-plane deviations of the B/C atoms from ideal positions are less than a third of these values, contrasting sharply with the behavior of the Li atoms, which show large in-plane displacements of ∼0.2 Å, with out-of-plane displacements almost 1 order of magnitude smaller; that is, the B/C atoms predominantly show out-of-plane displacements, the Li predominantly in-plane, in agreement with the interpretation of the refined anisotropic displacement parameters as resulting from static disorder. This is also consistent with the increase in size of the Li displacement parameters as the Li concentration decreases.

These local structural relaxations in response to Li loss are significant but do not change the density of states noticeably from the rigid band prediction based on a perfect, unrelaxed Li_xBC structure with planar sheets (Figure 8, panels (i) and (ii), shows the projected densities of states for C and B, respectively, in $Li_{0.5}BC$). In particular, both σ and π states coexist at E_F in the buckled structures, and thus, the similarity in electronic structure with MgB_2 is not lost despite the pronounced structural change. Further DFT calculations were therefore carried out to reveal and quantify the chemical driving force for the expulsion of B from highly Li deficient materials and to discover whether related structural relaxation could account for the failure to observe superconductivity in the Li_xBC family.

As boron expulsion is observed experimentally at high levels of Li loss, the energetic origin of this was investigated. Figure 9 shows the DFT calculations of the energy of formation of Li_xBC phases; it is notable that these materials are predicted to be thermodynamically unstable with respect to the elements when the Li content decreases below 0.4. More strikingly, the DFT calculations demonstrate that C-rich solids such as $LiBC_3$, a compound isoelectronic with graphite and very close in composition to experimentally observed $Li_{0.45(2)}B_{0.49(1)}C_{1.51(1)}$ (sample IX, Table 1), are calculated to be considerably more thermodynamically stable. Calculations on four different model structures of $LiBC_3$ all predict a crossover to stability of this C-enriched phase at Li contents very close to those where the

---

(23) Pronin, A. V.; Pucher, K.; Lunkenheimer, P.; Krimmel, A.; Loidl, A. *Phys. Rev. B* **2003**, *67*, 13.

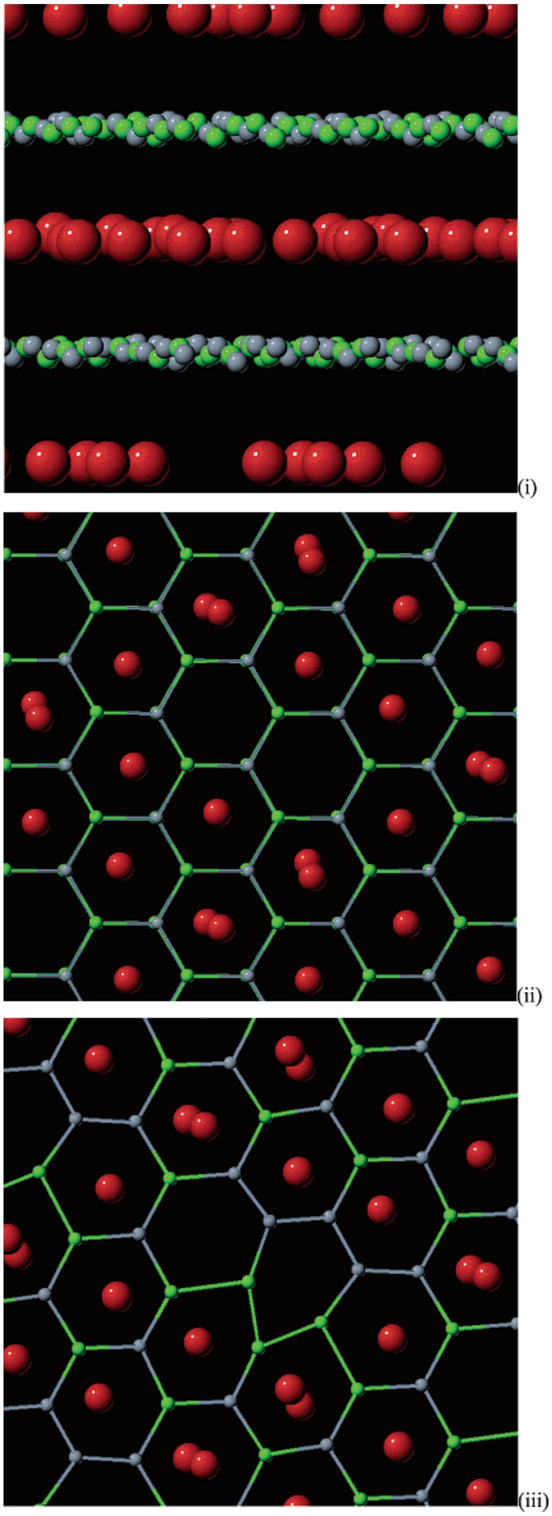

Figure 7. Relaxed structure of Li$_x$BC (x = 0.5) according to DFT calculations (Li red, B green, C gray). (i) The view parallel to the layers shows the long-period buckling of the Li$_x$BC layers, whereas (ii) the perpendicular view reveals the in-plane displacements of the Li species. (iii) The formation of B−B and C−C bonds upon B/C site swapping around a Li vacancy in Li$_{0.5}$BC.

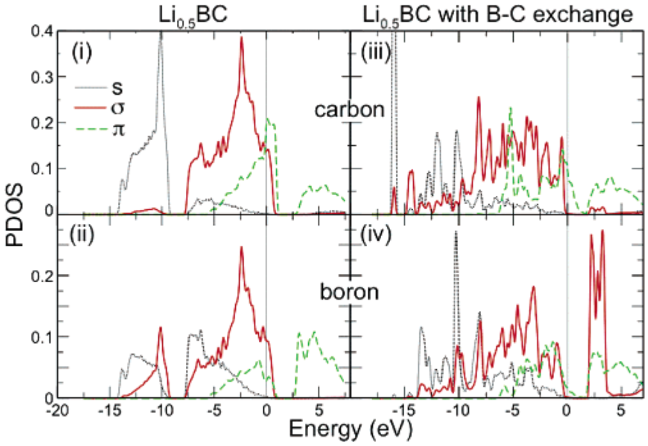

Figure 8. Projected density of states versus energy relative to the Fermi energy for carbon and boron atoms at a Li vacancy site in Li$_{0.5}$BC for the structure shown in Figure 7. Panels (i) and (ii) are for the unswapped structure showing clearly the rigid band behavior where the Fermi level moves into an essentially undistorted LiBC density of states. Panels (iii) and (iv) are for the structures in which the BC layers contain swapped carbon and boron sites, showing the depletion of the σ states at the Fermi energy. The σ states are removed from the Fermi level at every B and C atom in the swapped structure, not solely those neighboring the vacancy.

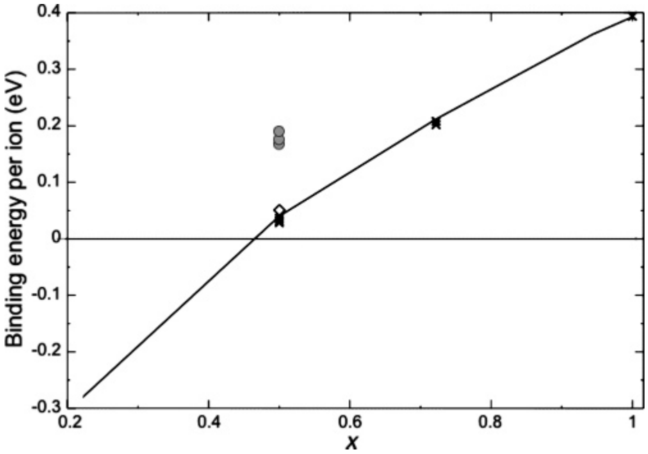

Figure 9. Computed binding energy per ion (total energy of compound minus total energy of elements) of Li$_x$BC versus Li content, x. The solid line shows results for the most favorable Li ordering, crosses indicate results obtained with some alternative orderings; that is, the solid line is not a guide to the eye but contains the outcome of calculations. The diamond indicates the binding energy of a favorable swapped structure for Li$_{0.5}$BC, whereas the circles are for 4 LiBC$_3$ structures (2 essentially degenerate), showing the strong favoring of B expulsion as Li loss increases.

expulsion of B from the layers is observed experimentally. This does not preclude kinetically controlled synthesis of metastable phases with B:C ratios of unity, but the calculations show the clear thermodynamic driving force for the experimentally observed B expulsion as the lithium content is reduced and the electron count is changed from that required for equivalence with graphite.

The electronic structure of LiBC$_3$ is quite dissimilar from that predicted for Li$_x$BC and is much closer to that of graphite. This suggests that important chemically driven electronic structure changes may occur before the change in layer composition. In particular, the observation of a group of phases with cell volumes (Figure 3) between the lightly Li doped and B-deficient groups, and the observation that B loss necessarily forms C−C bonds, prompted an investigation of the energetics of modifying the layer by swapping B and C, which also generates C−C near neighbor pairs.

Figure 10 shows that the energy of a B/C swap decreases very strongly as the Li content is reduced. In LiBC itself, there is a strong energy penalty of 1.7 eV for B/C site swaps within the layer. Structures with B and C swapped actually become

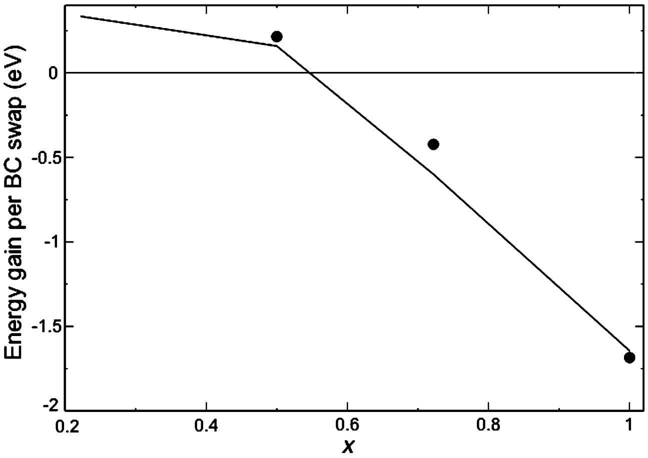

Figure 10. Energy gained on swapping adjacent B and C atoms within a layer versus Li content. Results for a single swap are shown by the solid line, and circles indicate energy per swap for 4 swaps around a Li vacancy site. Swaps for non-nearest-neighbors are unfavorable (as are swaps in Li rich regions) even for low *x* because this results in a B coordinated to three B neighbors. As for Figure 9, solid lines represent the outcome of calculations and are not guides to the eye.

favorable when the Li content decreases below 0.55. Swaps are only favored in the immediate vicinity of a Li vacancy (they are energetically unfavorable in regions where the vacancy concentration is close to zero) and act as a driving force for local vacancy clustering; that is, B/C swapping and Li vacancy formation are causally linked when the Li content decreases below 0.55.

The favored structures contain some B atoms coordinated to one C and two B neighbors, with the B−B bonds (∼1.6 Å) being considerably longer than the B−C (1.46 Å) or the C−C (1.41 Å) bonds, as shown in Figure 7(iii). Structures in which B has 3 B and no C neighbors are unfavorable and will limit the extent to which loss of B/C alternation is possible; when this limit is reached, it then becomes favorable to expel B from the structure. Qualitatively, the formation of B−B bonds is a mechanism to accommodate the electron deficiency within the layers. The partial charge on B is positive in “unswapped” $Li_{0.5}BC$ with perfect B/C alternation and becomes close to that on C in the lower energy swapped structure. The layer buckling observed in the unswapped structures is retained in the relaxed structures of the B/C swapped materials, and thus the enhanced displacement parameter anisotropy can be accounted for.

Figure 8, panels (iii) and (iv), shows the projected density of states for the swapped B and C atoms. The electronic structure in the swapped materials is robust to the precise structure used in the calculations; $N(E_f)$ is reduced, with states transferred from the vicinity of the Fermi level both to higher energies and to occupied states at lower energies, resulting in the filling in of the pronounced gaps in the pristine LiBC density of states which arise from the B/C alternation. In detail, we can see that, although the π states still span the Fermi energy, the introduction of B−B and C−C bonding splits the σ states at the Fermi energy. Some states, involved in B−B nearest-neighbor bonding, are transferred to higher energy, whereas the remainder of the σ states are pulled down in energy to become fully occupied. This occurs across the whole BC sheet, not just near the vacancy, irrespective of the precise arrangement of Li surrounding the vacancy; that is, there are essentially no σ states at the Fermi energy in the swapped structure. This main band of σ states, crucial to the superconductivity of MgB_2, is further dragged down in energy as B is expelled from the lattice. For $LiBC_3$, the σ band edge is pulled down ∼1.4 eV below the Fermi energy, further decreasing to −2.9 eV in pure graphite.

Discussion

It is significant to note that sample I with complete Li occupancy is single phase $Li_{1.00}BC$. The loss of lithium by high-temperature deintercalation is associated with phase separation. The evolution of cell volume, structure, and phase assemblage as Li is removed from LiBC indicates that a rigid-band doping to afford a range of Li_xBC phases is not achieved: the observation of two distinct clusters of Li_xBC phases followed by the expulsion of B to afford carbon-rich layered structures (Figure 3) indicates that the structure and composition respond strongly to loss of Li.

The refined average structures of the materials suggest considerable evolution in the local structure as the lithium content decreases, reflected in the anisotropic displacement parameters (Table 4) which change in distinct ways for the BC layer and interlayer Li atoms. The anisotropic displacement parameters for Li become large parallel to the layers ($U_{11}(Li)/U_{33}(Li)$ is 0.86 in LiBC (Figure 1a) but becomes 5.1 in $Li_{0.56(2)}BC$ (Figure 1b)). The BC layers themselves display enhanced out-of-plane displacements (U_{33}/U_{11} at room temperature is 2.96 for LiBC and 6.15 for $Li_{0.56(2)}BC$). The static component of U_{33} (estimated by extrapolation of $U_{33}(T)$ to 0 K) corresponds to an rms out of plane displacement of 0.15Å, in contrast to 0.06Å for $Li_{0.904(8)}BC$. The rms static in-plane displacement for $Li_{0.56(2)}BC$ is 0.07Å.

Resistivity measurements on the biphasic materials with $m > 0.5$ show that removal of Li does produce drastic enhancement of the conductivity, as required by the DFT models for the electronic structure of the Li_xBC phases. The synthesis thus gives access to sufficient hole doping to produce enhanced conductivity, but the resulting materials are not superconductors. The only explanation the experimental observations can offer based on this evidence for the absence of superconductivity in the system is the role of the static disorder. This disorder would not prevent the formation of highly conducting material on oxidation of the layers (Figure 6). In particular, the DFT calculations show that both σ and π states are present at the Fermi level of the hole-doped materials despite the significant, experimentally validated B/C layer buckling (Figure 8, panels (i) and (ii)). Therefore, the electronic structure analogy with MgB_2 survives the layer buckling, and the original predictions of high-temperature superconductivity in Li_xBC should remain valid.

The loss of lithium necessarily causes the formal layer electron count to deviate from that of graphite. This in turn can drive significant bonding changes within the layer, as revealed experimentally by the expulsion of boron at the highest levels of Li loss. Qualitatively, C enrichment of the layer combats the loss of electrons donated from interlayer Li and returns the electronic structure toward that of graphite. Quantitatively, DFT predicts a declining stability of Li_xBC with respect to the elements as x decreases and a crossover to C-rich phases with electronic structures similar to that of graphite; that is, there is no coexistence of σ and π states at the Fermi level in the materials formed by B expulsion with C-rich layers, which instead have a graphite-like electronic structure which would not be expected to produce superconductivity at above 40 K. These theoretical results are consistent with the idea that there is a limit to the ability of the BC sheet to accommodate hole doping. The instability of the BC sheet to B loss places an experimental lower bound on the extent to which rigid band doping is applicable in the Li_xBC system.

Both theory and experiment thus point to the $Li_{0.5}BC$ composition, originally identified as a candidate for high-temperature superconductivity, as close to the crossover stability point between hole-doped BC layers and graphite-like C-rich systems with an electronic structure different to that of the MgB_2 superconductor. This dramatic change in electronic structure, with the loss of the unique features associated with superconductivity in MgB_2 itself, explains why the group of highly Li-deficient $Li_xB_{1-y}C_{1+y}$ phases are not superconducting. It further suggests that a search for structural features premonitory to the compositional change in the BC layer might reveal how the electronic structure would be significantly modified from the rigid band prediction before the expulsion of B. The change in B:C ratio introduces C−C bonds that are not present in LiBC. Any relaxation of the strict alternation of B and C within the layers of LiBC would be expected to have a dramatic effect on the electronic structure of the system and would introduce C−C bonds similar to those formed by B loss. As $Li_{0.5}BC$ has been shown to be at the limits of the stability of the alternating atom sheet structure, with both theory and experiment identifying B loss as the stabilizing mechanism, we investigated whether the related structural relaxation of B/C interchange was possible in the hole-doped materials with a B:C ratio of 1.

The B/C swaps remain unfavorable at low Li deficiency (by >0.4 eV for $x = 0.72$), which may account for the observed composition gap between $x = 0.56$ and 0.9 (Figure 3). The $0.9 < x < 1$ region represents the composition range over which the unaltered BC sheet can accommodate hole doping without B/C swapping or B expulsion. Once the vacancy concentration exceeds this level, B/C swapping becomes energetically favorable and cooperative interaction between the location of Li vacancies and B/C site swaps favors the formation of considerably more Li-deficient phases around the $x = 0.5$ composition. Further Li loss then leads to the expulsion of B to restore the electron count within the sheet to be closer to that of graphite. The B/C swaps can thus be seen as premonitory to the bulk expulsion of B from the layers.

As expected, the changes in bonding patterns that drive the rearrangements within the BC layers strongly affect the electronic structure. This is consistent with the idea that these B/C swaps are the precursor to the expulsion of B to form a material isoelectronic with graphite. The effect of these swaps on the electronic structures in the vicinity of the Fermi level is to qualitatively differentiate the highly Li-deficient Li_xBC phases from MgB_2. Although the band structures are still metallic due to the π electrons which remain at E_F, consistent with the experimental observation of a significant increase in conductivity on doping, the σ states no longer coexist with these π states at E_F. B−B bonding states move above E_F, whereas C−C states move below, effectively removing the two-band nature at the Fermi level. It should be emphasized that this qualitative difference from MgB_2 (removal of the σ states from the Fermi level) is responsible for the suppression of superconductivity, rather than the simple reduction in the density of states at the Fermi level, $N(E_F)$. The predicted T_c using the McMillan or Dynes equation used in the original estimates of enhanced transition temperatures is reduced from 105 K to ∼10 K, but not suppressed completely. Thus, the more dramatic change to the electronic structure identified by DFT calculations is required to account for the absence of superconductivity.

The absence of superconductivity in Li_xBC can thus be traced to the evolution of the electronic and structural response of the (BC) sheet in LiBC to the “hole doping” produced by Li loss. The response evolves from rigid band doping for $0.9 \leq x \leq 1$ to B/C swapping for $0.45 \leq x \leq 0.55$ to B expulsion for lower Li contents; these two structural changes, producing the three distinct groups of experimentally observed phases in Figure 3, both result in reduction of the density of states at the Fermi level and an electronic structure more similar to that of graphite. The DFT calculations demonstrate that in the vicinity of the predicted high T_c composition of $Li_{0.5}BC$ the observation of significantly enhanced conductivity without superconductivity can be rationalized as the existence of a hole-doped material with a nonzero density of states at the Fermi level but without the coexistence of σ and π states which gives the unique superconducting behavior of MgB_2. This influence of chemical bonding on the structural rearrangements defeats the rigid band predictions of superconductivity in the doped materials. This is a fundamental difference between the extended s/p band systems and d-band materials such as the copper oxides where the tolerance of open shell electronic structures at a wide range of electron counts allows quasi-rigid band doping to operate. In the comparison between doped LiBC and superconducting MgB_2, it is the extra structural degree of freedom due to the presence of both B and C in the nonmetal layers of LiBC which prevents the borocarbide from displaying the structural rigidity required to imitate the electronic structure of the pure boride. Synthetic routes designed to prevent layer rearrangement during the growth of Li_xBC will need to be developed to access superconductivity in this system.

Acknowledgment. We thank EPSRC for funding under GR/R53999 and EP/C511794. A.M.F. thanks the Royal Society for a University Research Fellowship. We are grateful to Dr. W. Hofer for help with the VASP calculations. We thank Dr. J. Sloan and Dr. V. Stolojan of the Advanced Technology Institute, University of Surrey for the EELS measurements.

Supporting Information Available: Variation of unit cell dimensions with composition at 5 and 973 K. Rietveld refinement of synchrotron X-ray data of sample X. Variation of U_{iso}(Li) with composition. Variation of U_{11}(B/C) with composition. Comparison of refinement of sample XI in $P6/mmm$ and $P6_3/mmc$ space groups. This material is available free of charge via the Internet at http://pubs.acs.org.

JA0578449